Accepted Manuscript

International Journal of Modern Physics C

Article Title:	Hall current, Newtonian heating and second order slip effects on convective magneto-micropolar fluid flow over a sheet
Author(s):	Muhammad Kamran, Benchawan Wiwatanapataphee, Kuppalapalle Vajravelu
DOI:	10.1142/S0129183118500900
Received:	13 April 2018
Accepted:	09 August 2018
To be cited as:	Muhammad Kamran, Benchawan Wiwatanapataphee, Kuppalapalle Vajravelu, Hall current, Newtonian heating and second order slip effects on convective magneto-micropolar fluid flow over a sheet, *International Journal of Modern Physics C*, doi: 10.1142/S0129183118500900
Link to final version:	https://doi.org/10.1142/S0129183118500900

International Journal of Modern Physics C

Hall current, Newtonian heating and second order slip effects on convective magneto-micropolar fluid flow over a sheet

Muhammad Kamran*, Benchawan Wiwatanapataphee†
Department of Mathematics and Statistics,
Curtin University of Technology,
GPO Box U1987, Perth 6845 Australia
**muhammad.kamran@curtin.edu.au*
†*b.wiwatanapataphee@curtin.edu.au*

Kuppalapalle Vajravelu
Department of Mathematics,
University of Central Florida,
Orlando, FL 32816, USA
kuppalapalle.vajravelu@ucf.edu

Received Day Month Year
Revised Day Month Year

This research deals with an analysis of the Hall current effect on the mixed convective magneto-micropolar fluid flow over a permeable stretching/shrinking sheet. Impact of the Newtonian heating parameter is analysed in the slip flow regime. The non-linear equations of the fluid flow are derived with the help of a similarity transform and its solutions are obtained by Optimal Homotopy Analysis Method (OHAM). For limiting cases, obtained results are in excellent agreement with the available exact and numerical results in the literature. The graphical and tabular representations of the obtained results show significant effects of the physical parameters on the magneto-micropolar fluid flow and heat transfer characteristics. In particular, it is observed that, as the sheet stretches, a change in the Hall current parameter yields a higher horizontal velocity component for the lower value of the magnetic field parameter; while it produces a higher and shorter transverse velocity profile at high intensity of the magnetic field. In MHD generators, Hall effects are an important consideration to analyse the heat transfer phenomenon with high temperature conducting fluids.

Keywords: Hall current; Newtonian heating; magneto-micropolar fluid; stretching/shrinking sheet; slip flow.

PACS Nos.: 52.65.Kj, 44.25.+f, 44.05.+e.

Nomenclature

*Corresponding author.

A	constant coefficient for mean free path	$\vec{B}$	magnetic field vector
B	square of constant mean free path, m^2	B_o	transverse magnetic field, $Wb\ m^{-1}$
c_p	specific heat at constant pressure, $JK^{-1}Kg^{-1}$	C_f	local skin friction coefficient
d	molecular mean free path, m	$\vec{E}$	electric field vector
e	electric charge, C	f	dimensionless velocity
f_w	dimensionless suction/injection parameter	g	gravitational acceleration, ms^{-2}
Gr_x	dimensionless local Grashof number	h_s	surface heat transfer coefficient, $Wm^{-2}K^{-1}$
h	dimensionless micro rotational velocity	$\vec{J}$	electric current density vector
j	microinertia per unit mass, m^2	K	dimensionless material parameter
k	thermal conductivity, $Wm^{-1}K^{-1}$	k_n	Knudsen number
l	constants	M	dimensionless Magnetic field Parameter
m	Hall Parameter	M_x	local wall couple stress
n_e	number of charge on the electron density	Nu	local Nusselt number
Pr	dimensionless Prandtl number	Re_x	dimensionless local Reynolds number
s	stretching/ shrinking constant	T	fluid temperature, K
u	horizontal velocity component, ms^{-1}	$\vec{V}$	velocity vector
v_o	suction/injection velocity, ms^{-1}	x	horizontal direction, m
y	transverse directions, m	z	perpendicular to x and y, m

Greek symbols

α	dimensionless first order slip parameter	β	dimensionless second order slip parameter
β_T	coefficient of thermal expansion, K^{-1}	γ	spin gradient viscosity coefficient, $Kgms^{-1}$
δ	dimensionless Newtonian heating parameter	ϵ	momentum accommodation coefficient
θ	dimensionless temperature	λ	dimensionless buoyancy parameter
μ	dynamic viscosity, Nsm^{-2}	ν	kinematic viscosity, m^2s^{-1}
ψ	stream function, m^2s^{-1}	ρ	fluid density, Kgm^{-3}
χ	microrotation viscosity,$Kgm^{-1}s^{-1}$	ω	micro rotational velocity (cartesian), ms^{-1}

Subscripts

w	wall	∞	free stream.

1. Introduction

The theory of micropolar fluid flow, in which the fluid consists of the micro-structured particles with non-symmetric stress tensor, was presented by Eringen[1,2]. It explains the various concepts of fluid flow such as micro-rotational inertia and micro-rotational effects, which are not reported in the theory of the classical fluid mechanics. Animal blood, liquid crystal, colloidal fluid and fluids with certain additives are a few examples of the micropolar fluid. In the early decades, the theory of micropolar fluid has been used to investigate the influence of micro-structured particles on the rigid boundary layer[3] and heat conducting effects[4,5] on the micropolar fluid flow. Furthermore, research monographs reported by Lukaszewicz[6] and Eringen[7] explain the mathematical theory and applications of the micropolar fluid flow in the literature.

Recently, many investigations on the micropolar fluid flows have been carried out by analysing the variable heat flux[8], Magnetohydrodynamics (MHD) flow[9,10], non-linear power-law diffusion flow over the stretching sheet[11], nonlinearly shrinking/stretching sheet[12], flow in a differentially heated irregular cavity[13], square and wavy cavities[14,15] free convective flow over circular cylinder[16], and even over a permeable vertical cone[17]. From the above mentioned physical and engineering problems, it is observed that the micropolar fluid flow plays an important role in the chemical, manufacturing and biomedical industries, and results in a variety of applications such as crystal growing, paper production, polishing artificial organs, etc.

Moreover, the theory of micropolar fluids has also been extended to the electrically conducting fluids in a magnetic field which has numerous engineering applications in oil and gas extraction, chemical processing, Hall and MHD generators[18], please see in Ref. 18. More specifically, when an electric current passes through a conductor under the influence of a strong transverse magnetic field, then moving charged particles come under the influence of the magnetic force which causes to lean them to either side of the conducting material. Due to this drift or gyration of charged particles, the electric conductivity is reduced to produce another transverse current named as Hall current, and this phenomenon is called the Hall effect. Hall effect usually occurs in conducting solids, liquids as well as ionised gases. In last few decades, the convective heat models of the micropolar fluid flow have been studied by taking into account within the influence of the Hall current. Eldahab and El-Aziz[19] have analysed the impact of the Ohmic heating and the Hall current on the rotating cone immersed in a magneto-micropolar fluid flow. Thermal instability of the micropolar fluid flow under the influence of the Hall current has been reported by Rani and Tomar[20]. The combined effects of the Hall current and the thermal radiation on the heat and mass transfer of the micropolar fluid flow in the rotating system within the influence of heat generation and chemical reaction have been studied by Pal et al.[21]. Furthermore, Yang and Wang[22] investigated the magnetic field effect on power-law non-Newtonian fluid flow passing through a rectangular channel by using a multiple-relaxation-time lattice Boltzmann method.

In many engineering applications, it has been observed that the fluid particles close to the solid surface slip along the surface due to their finite tangential velocity. This flow regime is termed as a slip-flow regime in which shear stress depends on the slip velocity. This effect cannot be ignored. The study of the slip-flow regime has many technological applications, e.g., refrigerating coils, transmission lines, electric transformers, heating elements, polishing artificial heart valves and internal cavities. Wu[23] derived the second order slip model for the rarefied gas flow for arbitrary Knudsen number with the help of the kinetic theory. From the obtained results, it was investigated that Wu's slip flow model is much preferable to consider as compared to the 1^{st} order, 1.5^{th} order or 2^{nd} order slip flow models, please see in Ref. 23. Furthermore, Wu's slip flow model has been extended to the quiescent fluid[24,25,26,27] and micropolar fluid flows[28,29,30] with their analytical or numerical investigations.

Above mentioned reports govern to investigate the influence of the Hall current and the Newtonian heating on the mixed convective magneto-micropolar fluid flow over a stretching/shrinking porous sheet with the second order slip flow model. In this paper, we study a steady mixed convection flow of an incompressible magneto-micropolar fluid over the stretching/shrinking porous sheet with 2^{nd} slip flow condition[23] and neglecting the effects of the induced magnetic field. The governing partial differential equations of the coupled fluid flow and heat transfer in the presence of the electromagnetic field are presented here. A suitable similarity transformation reduces the governing equations to the dimensionless nonlinear ordinary differential equations (ODEs). The transformed nonlinear ODEs under the prescribed boundary conditions are solved analytically by using OHAM. The influences of the governing flow parameters along with the Hall current and Newtonian heating are investigated. The remaining paper is organised as follows, section 2 proposes a mathematical model of the governing flow and introduces a similarity transformation analysis to obtained a similarity solution of the problem. In section 3, an approximate analytical solution using OHAM is derived. Furthermore, the proceeding sections concern with the study validation, results and discussion, and conclusion of the conducted research.

2. Governing Equations

Here, it is considered a steady state mixed convective flow of an incompressible magneto-micropolar fluid passing over a permeable stretching/shrinking surface with second order slip velocity. Stretching/shrinking behavior is described by the velocity $u = su_w(x)$, where $u_w(x) = ax$ and a is a positive dimensional constant along the axis of flow. This MHD fluid flow is taken along the x-axis and the uniform magnetic field (B_o) is supplied in a direction normal to the flow field, as shown in Fig. 1, with neglecting the induced magnetic field[31]. It is also assumed that the Newtonian heating causes to generate the natural convection flow, i.e., heat transfer rate on the stretching/shrinking sheet is taken to be proportional to the surface

temperature[32]. In this MHD flow, Hall effect induces a Hall current which causes to produce a force in the direction (along with z-axis) normal to the steady flow of the electrically conducting fluid and magnetic force. Therefore, the prescribed mathematical model becomes three dimensional. For simplicity, no changes are considered in the fluid flow and heat transfer quantities along the z-axis, so the fluid model reduces to two-dimensional flow. In the absence of the ion-slip and pressure diffusion effects, the generalized Ohm's law with Maxwell's equations[31,33,34] can be written as

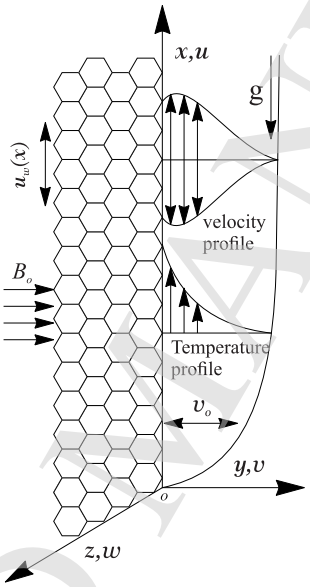

Fig. 1. Flow model.

$$\vec{J} = \sigma\left(\vec{E} + \vec{V} \times \vec{B} - \frac{1}{en_e}\vec{J} \times \vec{B}\right), \tag{1}$$

$$\bigtriangledown \times \vec{B} = \mu_o \vec{J}, \tag{2}$$

$$\bigtriangledown \cdot \vec{B} = 0, \tag{3}$$

$$\bigtriangledown \times \vec{E} = 0, \tag{4}$$

$$\bigtriangledown \cdot \vec{J} = 0, \tag{5}$$

where $\vec{J}$ is an electric current density vector with cartesian components (J_x, J_y, J_z), μ_o is the permeability of free space , $\sigma = n_e e^2 \tau / m_e$ is the electrical conductivity in which n_e is the number of charge on the electron density; e is the electron charge; τ is the electron collision time; m_e is the electron mass; $\vec{E} = (E_x, E_y, E_z), \vec{V} = (u, v, w)$, and $\vec{B} = (0, B_o, 0)$ are vectors of the electric field, velocity, and magnetic induction,

respectively. It is considered that the stretching/shrinking sheet is electrically non-conducting material which gives $J_y = 0$ everywhere in the flow regime. Moreover, flow field is assumed without any applied voltage which results in $\vec{E} = 0$ from Eq. (4). Hence the Eq. (1) yields

$$J_x = \frac{\sigma B_o}{1+m^2}(mu - w), \tag{6}$$

$$J_z = \frac{\sigma B_o}{1+m^2}(u + mw), \tag{7}$$

where $m = \sigma B_o / e n_e$ is the Hall parameter. Furthermore, in the absence of viscous dissipation and Ohmic heating, the usual Boussinesq approximation is introduced to obtained the mathematical form of governing equations[33] as

$$\frac{\partial u}{\partial x} + \frac{\partial v}{\partial y} = 0, \tag{8}$$

$$u\frac{\partial u}{\partial x} + v\frac{\partial u}{\partial y} = \frac{\mu+\chi}{\rho}\left(\frac{\partial^2 u}{\partial y^2}\right) + \mathrm{g}\beta_T\left(T - T_\infty\right) + \frac{\chi}{\rho}\left(\frac{\partial \omega}{\partial y}\right) - \frac{B_o}{\rho}J_z, \tag{9}$$

$$u\frac{\partial w}{\partial x} + v\frac{\partial w}{\partial y} = \frac{\mu+\chi}{\rho}\left(\frac{\partial^2 w}{\partial y^2}\right) + \frac{B_o}{\rho}J_x, \tag{10}$$

$$u\frac{\partial \omega}{\partial x} + v\frac{\partial \omega}{\partial y} = \frac{\gamma}{\rho j}\left(\frac{\partial^2 \omega}{\partial y^2}\right) - \frac{\chi}{\rho j}\left(2\omega + \frac{\partial u}{\partial y}\right), \tag{11}$$

$$u\frac{\partial T}{\partial x} + v\frac{\partial T}{\partial y} = \frac{k}{\rho c_p}\left(\frac{\partial^2 T}{\partial y^2}\right), \tag{12}$$

with boundary conditions

$$\left.\begin{aligned} u = s u_w(x) + u_{\mathrm{slip}}; v = v_o; w = 0; \omega = -n\frac{\partial u}{\partial y}; k\frac{\partial T}{\partial y} = -h_s T \text{ at } y = 0, \\ u \to 0;\ w \to 0;\ \omega \to 0;\ T \to T_\infty \text{ as } y \to \infty. \end{aligned}\right\} \tag{13}$$

The spin gradient viscosity is determined by $\gamma = (\mu + \chi/2)\, j = \mu\,(1 + K/2)\, j$ for the material parameter $K = \chi/\mu$ and the microinertia density $j = \nu/a$ [35]. Moreover, $v_o > 0$ is the suction and $v_o < 0$ is the injection velocities of the permeable sheet. The constant n has assigned in the range of 0 to 1, please see the Ref. 36. Furthermore, u_{slip} is slip velocity of the stretching ($s > 0$)/shrinking ($s < 0$) sheet, which is given by Wu [23] as

$$u_{\mathrm{slip}} = \frac{2}{3}\left(\frac{3 - \epsilon l^3}{\epsilon} - \frac{3}{2}\frac{1 - l^2}{k_n}\right) d\frac{\partial u}{\partial y} - \frac{1}{4}\left(l^4 + \frac{2}{k_n^2}(1 - l^2)\right) d^2\frac{\partial^2 u}{\partial y^2} = A\frac{\partial u}{\partial y} + B\frac{\partial^2 u}{\partial y^2},$$

where $l \simeq min(1/k_n, 1)$ which reads between 0 to 1 for all values of the Knudsen (k_n) number and the ϵ is defined between 0 to 1. Furthermore, d is positive and B is consequently negative in magnitude. However, by introducing the non-dimensional similarity variables

$$\eta = \sqrt{a/\nu}\, y,\ \psi = \sqrt{a\nu} x f(\eta),\ w = axg(\eta),\ \omega = \sqrt{a/\nu} a h(\eta) \text{ and } \theta(\eta) = \frac{T - T_\infty}{T_\infty}$$

with velocity components $u = \partial\psi/\partial y$ and $v = -\partial\psi/\partial x$ in which the stream function (ψ) usually satisfies the equation of the conservation of mass Eq. (8). The governing equations (Eqs. (9)–(12)) are transformed into a set of non-linear ordinary differential equations as follows:

$$(1+K)f''' - (f')^2 + ff'' + \lambda\theta + Kh' - \frac{M}{1+m^2}(f' + mg) = 0, \tag{14}$$

$$(1+K)g'' + fg' - f'g + \frac{M}{1+m^2}(mf' - g) = 0, \tag{15}$$

$$(1+K/2)h'' - f'h + fh' - K(2h + f'') = 0, \tag{16}$$

$$\theta'' + Prf\theta' = 0. \tag{17}$$

The boundary conditions Eq. (13) become

$$\left.\begin{aligned} f = f_w;\ f' = s + \alpha f'' + \beta f'''; \ g = 0;\ h = -nf'';\ \theta' = -\delta(1+\theta) \text{ at } \eta = 0, \\ f' \to 0;\ g \to 0;\ h \to 0;\ \theta \to 0 \text{ as } \eta \to \infty, \end{aligned}\right\} \tag{18}$$

where prime($'$) is used for the derivative with respect to η. $\lambda = Gr_x/Re_x$ is the buoyancy parameter for $Gr_x = \mathrm{g}\beta_T T_\infty x/a\nu$ (local Grashof number) and $Re_x = ax^2/\nu$ (local Reynolds number), $M = \sigma B_o^2/a\rho$ is the Magnetic field parameter, $Pr = \mu c_p/k$ represents the Prandtl number. Eq. (18) contains suction (> 0) or injection (< 0) parameter $f_w = -(a\nu)^{-\frac{1}{2}} v_o$, first order slip flow parameter $\alpha = A\sqrt{a/\nu} > 0$, second order slip flow parameter $\beta = Ba/\nu < 0$, and Newtonian heating parameter $\delta = (h_s/k)\sqrt{\nu/a}$.

Moreover, the physical quantities including local skin friction coefficients (C_{f_x} and C_{f_z}), local wall couple stress (M_x) and the local Nusselt number (Nu_x) are determined as follows:

$$C_{f_x} = \frac{-\tau_{w_x}}{\rho(u_w(x))^2} \text{ for } \tau_{w_x} = (\mu + \chi)\frac{\partial u}{\partial y} + \chi\omega\Big|_{y=0},$$

$$C_{f_z} = \frac{\tau_{w_z}}{\rho(u_w(x))^2} \text{ for } \tau_{w_z} = (\mu + \chi)\frac{\partial w}{\partial y}\Big|_{y=0},$$

$$M_x = \frac{-m_w}{\rho x(u_w(x))^2} \text{ for } m_w = \left(\mu + \frac{\chi}{2}\right) j\frac{\partial \omega}{\partial y}\Big|_{y=0},$$

$$Nu_x = \frac{-xq_w}{(T - T_\infty)} \text{ for } q_w = \frac{\partial T}{\partial y}\Big|_{y=0}.$$

Using the similarity transformation to make the above physical quantities dimen-

sionless, we have

$$\begin{aligned} C_{f_x} Re_x^{\frac{1}{2}} &= -\left(1+K-nK\right) f''(\eta)|_{\eta=0}\,, \\ C_{f_z} Re_x^{\frac{1}{2}} &= \left(1+K\right) g'(\eta)|_{\eta=0}\,, \\ M_x Re_x &= -\left(1+\frac{K}{2}\right) h'(\eta)\Big|_{\eta=0}\,, \\ Nu_x Re_x^{-\frac{1}{2}} &= \delta\left(1+\frac{1}{\theta(\eta)}\right)\Big|_{\eta=0}\,. \end{aligned}$$

3. OHAM Solution

An efficient approximate analytical technique, named Optimal Homotopy Analysis Method (OHAM), is used to solve the coupled nonlinear system of equations (Eqs. (14)–(17)) with boundary conditions in (Eq. (18)). This semi-analytical approach, proposed and developed by Liao [37,38,39], has an advantage on the perturbation and non-perturbation methods and has a great freedom to get the convergent series solution.

The homotopy series solutions corresponding to a set of the base function $\left\{\eta^r e^{-i\eta} | r \geq 0, i \geq 0\right\}$ can be expressed in the following form:

$$\left.\begin{aligned} f(\eta) &= \sum_{r=0}^{\infty}\sum_{i=0}^{\infty} a_{r,i}\eta^r e^{-i\eta}, \\ g(\eta) &= \sum_{r=0}^{\infty}\sum_{i=0}^{\infty} b_{r,i}\eta^r e^{-i\eta}, \\ h(\eta) &= \sum_{r=0}^{\infty}\sum_{i=0}^{\infty} c_{r,i}\eta^r e^{-i\eta}, \\ \theta(\eta) &= \sum_{r=0}^{\infty}\sum_{i=0}^{\infty} d_{r,i}\eta^r e^{-i\eta}, \end{aligned}\right\} \tag{19}$$

with the constant coefficients $a_{r,i}, b_{r,i}\, c_{r,i}$ and $d_{r,i}$. The set of initial solutions is chosen to be

$$\left.\begin{aligned} f_0(\eta) &= f_w + \frac{s(1-e^{-\eta})}{1+\alpha-\beta}, \\ g_0(\eta) &= 0, \\ h_0(\eta) &= \frac{sne^{-\eta}}{1+\alpha-\beta}, \\ \theta_0(\eta) &= \frac{\delta e^{-\eta}}{1-\delta} \quad ;\delta \neq 1, \end{aligned}\right\} \tag{20}$$

with the corresponding linear operators

$$\mathcal{L}_f = \frac{d^3}{d\eta^3} - \frac{d}{d\eta},\ \mathcal{L}_g = \frac{d^2}{d\eta^2} + \frac{d}{d\eta},\ \mathcal{L}_h = \frac{d^2}{d\eta^2} + \frac{d}{d\eta} \text{ and } \mathcal{L}_\theta = \frac{d^2}{d\eta^2} + \frac{d}{d\eta}, \tag{21}$$

satisfying the following properties

$$\left.\begin{aligned} \mathcal{L}_f\left[F_1 + F_2 e^{\eta} + F_3 e^{-\eta}\right] = 0, \\ \mathcal{L}_g\left[F_4 + F_5 e^{-\eta}\right] = 0, \\ \mathcal{L}_h\left[F_6 + F_7 e^{-\eta}\right] = 0, \\ \mathcal{L}_\theta\left[F_8 + F_9 e^{-\eta}\right] = 0, \end{aligned}\right\} \tag{22}$$

for arbitrary constants $F_i (i$ varies from 1 to 9). Let $q(\in [0,1])$ be the embedding parameter, $\hbar$ denote the non–zero auxiliary parameter and $H(\eta)$ be a non–zero auxiliary function. The zero–order deformation equations with corresponding non–linear functions $(\mathcal{N}_f, \mathcal{N}_g, \mathcal{N}_h, \mathcal{N}_\theta)$ can be written as

$$\left.\begin{aligned} (1-q)\mathcal{L}_f\left[\phi(\eta,q) - f_0(\eta)\right] = q\hbar_f H_f(\eta)\mathcal{N}_f\left[\phi(\eta,q), \varphi(\eta,q), \Phi(\eta,q), \Psi(\eta,q)\right], \\ (1-q)\mathcal{L}_g\left[\varphi(\eta,q) - g_0(\eta)\right] = q\hbar_g H_g(\eta)\mathcal{N}_g\left[\phi(\eta,q), \varphi(\eta,q), \Phi(\eta,q), \Psi(\eta,q)\right], \\ (1-q)\mathcal{L}_h\left[\Phi(\eta,q) - h_0(\eta)\right] = q\hbar_h H_h(\eta)\mathcal{N}_h\left[\phi(\eta,q), \varphi(\eta,q), \Phi(\eta,q), \Psi(\eta,q)\right], \\ (1-q)\mathcal{L}_\theta\left[\Psi(\eta,q) - \theta_0(\eta)\right] = q\hbar_\theta H_\theta(\eta)\mathcal{N}_\theta\left[\phi(\eta,q), \varphi(\eta,q), \Phi(\eta,q), \Psi(\eta,q)\right], \end{aligned}\right\} \tag{23}$$

with the following associated boundary conditions at $\eta = 0$ and $\eta \to \infty$, i.e.

$$\left.\begin{aligned} \phi(0,q) = f_w;\ \left.\frac{\partial\phi(\eta,q)}{\partial\eta}\right|_{\eta=0} = s + \alpha\left.\frac{\partial^2\phi(\eta,q)}{\partial\eta^2}\right|_{\eta=0} + \beta\left.\frac{\partial^3\phi(\eta,q)}{\partial\eta^3}\right|_{\eta=0}; \\ \left.\frac{\partial\phi(\eta,q)}{\partial\eta}\right|_{\eta\to\infty} \to 0;\ \varphi(0,q) \to 0;\ \varphi(\infty,q) \to 0;\ \Phi(0,q) = -n\left.\frac{\partial^2\phi(\eta,q)}{\partial\eta^2}\right|_{\eta=0}; \\ \Phi(\infty,q) \to 0;\ \left.\frac{\partial\Psi(\eta,q)}{\partial\eta}\right|_{\eta=0} = -\delta(1+\Psi(0,q));\ \Psi(\infty,q) \to 0, \end{aligned}\right\} \tag{24}$$

where $\hbar$ and $H(\eta)$ are chosen in a way that the series solutions converge at $q = 1$. Therefore,

$$\left.\begin{aligned} f(\eta) = f_0(\eta) + \sum_{p=1}^{\infty} f_p(\eta) q^p, \\ g(\eta) = g_0(\eta) + \sum_{p=1}^{\infty} g_p(\eta) q^p, \\ h(\eta) = h_0(\eta) + \sum_{p=1}^{\infty} h_p(\eta) q^p, \\ \theta(\eta) = \theta_0(\eta) + \sum_{p=1}^{\infty} \theta_p(\eta) q^p, \end{aligned}\right\} \tag{25}$$

in which

$$f_p(\eta) = \frac{1}{p!}\frac{\partial^p \phi(\eta,q)}{\partial q^p}\bigg|_{q=0},\ g_p(\eta) = \frac{1}{p!}\frac{\partial^p \phi(\eta,q)}{\partial q^p}\bigg|_{q=0},\ h_p(\eta) = \frac{1}{p!}\frac{\partial^p \varphi(\eta,q)}{\partial q^p}\bigg|_{q=0},$$
$$\theta_p(\eta) = \frac{1}{p!}\frac{\partial^p \Phi(\eta,q)}{\partial q^p}\bigg|_{q=0}.$$

Differentiating the zero-order deformation equations Eq. (23) p-times with respect to q and dividing by $p!$ yield the p^{th}–order deformation equations in the following form when $q = 0$:

$$\left.\begin{aligned}
\mathcal{L}_f\left[f_p(\eta) - \mathcal{X}_p f_{p-1}(\eta)\right] &= \hbar_f H_f(\eta)\mathfrak{R}_p^f(f_{p-1}(\eta), g_{p-1}(\eta), h_{p-1}(\eta), \theta_{p-1}(\eta)),\\
\mathcal{L}_g\left[g_p(\eta) - \mathcal{X}_p g_{p-1}(\eta)\right] &= \hbar_g H_g(\eta)\mathfrak{R}_p^g(f_{p-1}(\eta), g_{p-1}(\eta), h_{p-1}(\eta), \theta_{p-1}(\eta)),\\
\mathcal{L}_h\left[h_p(\eta) - \mathcal{X}_p h_{p-1}(\eta)\right] &= \hbar_h H_h(\eta)\mathfrak{R}_p^h(f_{p-1}(\eta), g_{p-1}(\eta), h_{p-1}(\eta), \theta_{p-1}(\eta)),\\
\mathcal{L}_\theta\left[\theta_p(\eta) - \mathcal{X}_p \theta_{p-1}(\eta)\right] &= \hbar_\theta H_\theta(\eta)\mathfrak{R}_p^\theta(f_{p-1}(\eta), g_{p-1}(\eta), h_{p-1}(\eta), \theta_{p-1}(\eta)),
\end{aligned}\right\} \quad (26)$$

with the associated boundary conditions at $\eta = 0$ and $\eta \to \infty$ as follows:

$$\left.\begin{aligned}
&f_p(0) = f_w,\ f_p'(0) = s + \alpha f_p''(0) + \beta f_p'''(0),\ g_p(0) = 0,\ h_p(0) = -n f_p''(0),\\
&\theta_p'(0) = -\delta(1 + \theta_p(0)),\ f_p'(\infty) \to 0,\ g_p(\infty) \to 0,\ h_p(\infty) \to 0,\ \theta_p(\infty) \to 0.
\end{aligned}\right\} \quad (27)$$

In Eq. (26),

$$\mathcal{X}_p = \begin{cases} 0 \text{ for } p \le 1,\\ 1 \text{ for } p > 1, \end{cases}$$

$$\mathfrak{R}_p^f(f_{p-1}(\eta), g_{p-1}(\eta), h_{p-1}(\eta), \theta_{p-1}(\eta)) = (1+K)f_{p-1}'''(\eta) + \sum_{i=0}^{p-1} f_i(\eta) f_{p-1-i}''(\eta) -$$
$$\sum_{i=0}^{p-1} f_i'(\eta) f_{p-1-i}'(\eta) + \lambda\theta_{p-1}(\eta) + K h_{p-1}'(\eta) - \frac{M}{1+m^2}(f_{p-1}(\eta) + m g_{p-1}(\eta)),$$

$$\mathfrak{R}_p^g(f_{p-1}(\eta), g_{p-1}(\eta), h_{p-1}(\eta), \theta_{p-1}(\eta)) = (1+K)g_{p-1}''(\eta) + \sum_{i=0}^{p-1} f_i(\eta) g_{p-1-i}'(\eta) -$$
$$\sum_{i=0}^{p-1} f_i'(\eta) g_{p-1-i}(\eta) + \frac{M}{1+m^2}(m f_{p-1}'(\eta) - g_{p-1}(\eta)),$$

$$\mathfrak{R}_p^h(f_{p-1}(\eta), g_{p-1}(\eta), h_{p-1}(\eta), \theta_{p-1}(\eta)) = (1+K/2)h_{p-1}''(\eta) + \sum_{i=0}^{p-1} f_i(\eta) h_{p-1-i}'(\eta) -$$
$$\sum_{i=0}^{p-1} f_i'(\eta) h_{p-1-i}(\eta) - K\left(2h_{p-1}(\eta) + f_{p-1}''(\eta)\right) \text{ and}$$

$$\mathfrak{R}_p^\theta(f_{p-1}(\eta), g_{p-1}(\eta), h_{p-1}(\eta), \theta_{p-1}(\eta)) = \theta_{p-1}''(\eta) + Pr\sum_{i=0}^{p-1} f_i(\eta)\theta_{p-1-i}'(\eta).$$

For the sack of simplicity, values of all auxiliary functions are set as

$$H_f(\eta) = H_g(\eta) = H_h(\eta) = H_\theta(\eta) = 1.$$

From Eq. (26), we then obtain the general solutions in the following form:

$$\left.\begin{aligned} f_p(\eta) &= f_p^*(\eta) + F_1 + F_2 e^{\eta} + F_3 e^{-\eta}, \\ g_p(\eta) &= g_p^*(\eta) + F_4 + F_5 e^{-\eta}, \\ h_p(\eta) &= h_p^*(\eta) + F_6 + F_7 e^{-\eta}, \\ \theta_p(\eta) &= \theta_p^*(\eta) + F_8 + F_9 e^{-\eta}, \end{aligned}\right\} \tag{28}$$

where $f_p^*(\eta),\ g_p^*(\eta),\ h_p^*(\eta)$ and $\theta_p^*(\eta)$ are particular solutions extracted by Eq. (26), and $F_i (i = 1, \cdots, 9)$ are determined by using Eq. (27).

It is noted that the particular solutions in Eq. (28) contain the four unknown convergence control parameters $\hbar_f, \hbar_g, \hbar_h$ and $\hbar_\theta$ which determine the convergence region for the Homotopy series solutions as derived in Eq. (28). Obviously, if values of the convergence control parameters are properly chosen, solutions in Eq. (28) may converges fast. So, we should determine the good enough values of these parameters so that the solutions in Eq. (28) converge fast enough. For brevity, the optimal values of the convergence control parameters can be determined with the help of average squared residual errors

$$\left.\begin{aligned} E_p^f &= \frac{1}{r}\sum_{j=0}^{r}\left[\mathcal{N}\left(\sum_{r=0}^{p} f_r(j\Delta\eta)\right)\right]^2, \quad E_p^g = \frac{1}{r}\sum_{j=0}^{r}\left[\mathcal{N}\left(\sum_{r=0}^{p} g_r(j\Delta\eta)\right)\right]^2, \\ E_p^h &= \frac{1}{r}\sum_{j=0}^{r}\left[\mathcal{N}\left(\sum_{r=0}^{p} h_r(j\Delta\eta)\right)\right]^2, \quad E_p^\theta = \frac{1}{r}\sum_{j=0}^{r}\left[\mathcal{N}\left(\sum_{r=0}^{p} \theta_r(j\Delta\eta)\right)\right]^2, \end{aligned}\right\} \tag{29}$$

in which $\Delta\eta = 10/r$ and $r = 20$ and the total squared residual error is $E_p^t = E_p^f + E_p^g + E_p^h + E_p^\theta$. Furthermore, computation software MATHEMATICA is used to solve the system of ODEs in Eqs. (14)–(17) with boundary conditions in Eq. (18).

3.1. *Optimal convergence Control parameters*

Homotopy analysis method has a freedom to control the convergence of the series solution by fixing the value of the non-zero convergence control parameter (auxiliary parameter). The values of the optimal convergence control parameters against sixth order of Homotopy approximations are presented in Table 2. It is found that as the order of the Homotopy approximation increases, the optimal convergence control parameters give the minimum of the total average squared residual error. Table 2 is computed for $K = \lambda = \alpha = s = 1,\ m = M = f_w = \delta = 0.1,\ \beta = -1,\ Pr = 2,\ n = 0.5$. Moreover, using the same parametric values (as used for Table 2), the average squared residual error is tabulated in Table 3 along with the computation time. A machine of 8 GB RAM and Intel(R) Core i7-4790 CPU with 3.60GHz processor is used. Furthermore, for the flexibility of results we fixed $\hbar_f = \hbar_g = \hbar_h = \hbar_\theta = \hbar$

and the curves of convergence control parameter ($\hbar$) are plotted and displayed in Figs. 2–3. The parametric values of Table 2 (or otherwise mentioned in the graph) are assigned to generate these graphs at 20^{th}-order of iterations of OHAM. In Fig. 2, it is to be noted that for stretching case ($s = 1$), curves are plotted at $\eta = 0$ while for shrinking case ($s = -1$) at $\eta = 30$ is used. It is observed that the $\hbar$-values can be chosen within the common admissible range of $-0.35 \leq \hbar < 0$ to analyse the effects of the prescribed parameters on the micropolar fluid flow. Moreover, the ($\hbar$) curve in Fig. 3 is used to validate the exact analytical results.

Table 2. Values of convergence control parameters.

p	$-\hbar_f$	$-\hbar_g$	$-\hbar_h$	$-\hbar_\theta$	E_p^t	CPU Time(s)
1	0.8932	0.55797	0.418652	0.087445	0.0006333	0.59
2	0.717632	0.347083	0.520176	0.5782	0.0000850	2.56
3	0.580908	0.254204	0.386921	0.442041	0.0000342	13.60
4	0.91244	0.431717	0.635011	0.447151	0.0000223	32.66
5	0.809656	0.106664	0.323863	0.404719	0.0000101	90.74
6	0.676212	0.312604	0.355828	0.425257	0.0000033	315.59

Table 3. Individual average squared residual error.

p	E_p^f	E_p^g	E_p^h	E_p^θ	CPU Time(s)
2	0.00713945	2.2622×10^{-7}	3.9966×10^{-4}	1.503×10^{-4}	0.55
4	0.00504071	1.0345×10^{-7}	9.3490×10^{-5}	9.683×10^{-5}	1.51
6	0.00339773	5.6185×10^{-8}	1.9300×10^{-5}	6.281×10^{-5}	3.37
8	0.00219339	3.6338×10^{-8}	5.2798×10^{-6}	4.167×10^{-5}	6.46
10	0.00135467	2.6144×10^{-8}	4.4309×10^{-6}	2.853×10^{-5}	11.09
12	0.00079764	1.9415×10^{-8}	4.8582×10^{-6}	2.013×10^{-5}	18.04
14	0.00044514	1.4220×10^{-8}	4.4657×10^{-6}	1.449×10^{-5}	28.16
16	0.00023340	1.0058×10^{-8}	3.4876×10^{-6}	1.052×10^{-5}	43.00
18	0.00011349	6.8116×10^{-9}	2.4045×10^{-6}	7.626×10^{-6}	64.66
20	0.00005016	4.4072×10^{-9}	1.4975×10^{-6}	5.493×10^{-6}	95.17

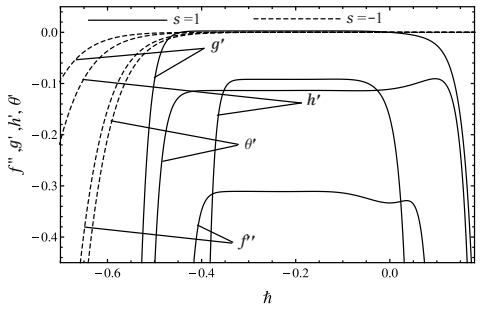

Fig. 2. $\hbar$-curves

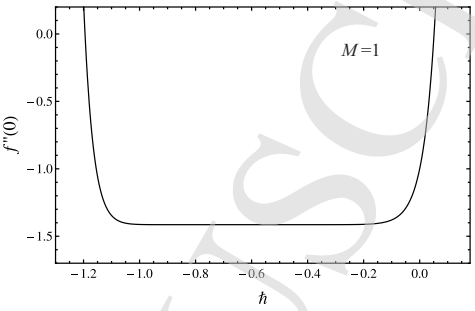

Fig. 3. $\hbar$-curve

4. Study Validation

In this section, the present study is validated with the exact solution of Eq. (14) and the already published numerical results of the Rosca and Pop [28]. Firstly, the special case arising from the Eq. (14) in which the forced convective ($\lambda = 0$) Newtonian ($K = 0$) fluid flow passing over an impermeable ($f_w = 0$) stretching sheet ($s = 1$) is considered in the absence of the slip flow condition ($\alpha = \beta = 0$) and the Hall effect ($m = 0$). This case yields the Eq. (14) as

$$f''' - (f')^2 + ff'' - Mf' = 0 \tag{30}$$

with boundary conditions $f(0) = 0, f'(0) = 1$, and $f'(\infty) = 0$ and it's exact solution, for $\Lambda = 2\sqrt{1+M}$, has the form

$$f(\eta) = \frac{1}{\Lambda}(2 - 2e^{-\Lambda\eta/2}) \tag{31}$$

which satisfies the boundary conditions. From Fig. 3 the auxiliary parameter $\hbar$ is chosen within the range of $-1 \leq \hbar \leq -0.1$. The solution in Eq. (31) is compared with the obtained OHAM solution at the 20^{th}-order of approximation in Table 4 for different values of the M which is found to be in excellent agreement.

Secondly, the accuracy of the OHAM results also assessed with the help of the numerical results presented by the Rosca and Pop[28]. In this comparison, magnetic field and Hall effects are not taken into account for shrinking case and again it is found to be in an excellent correspondence at $K = \alpha = 1,\ \lambda = m = M = 0,\ f_w = 3,\ s = \beta = -1$ and $n = 0.2$, in Fig. 4. In this comparison, the lower curve is sketched for f' at $\hbar = -0.095$ and upper curve is plotted for h at $\hbar = -0.13$.

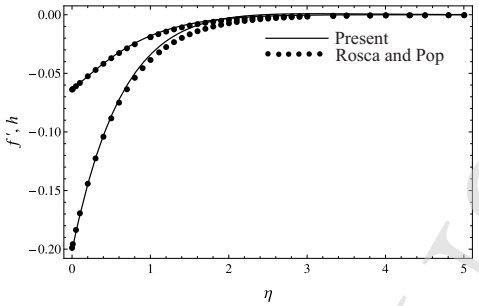

Fig. 4. validation with Rosca and Pop[28]

Table 4. Comparison with the exact solution for numerous values of M.

	Eq. (31)	Present			
M	$-f_e''(0)$	$-f''(0)$	$-\hbar$	E_f	CPU Time(s)
0.0	1	1	0.6	–	–
0.5	1.224744871391589	1.22474487139158	0.71	9.05×10^{-25}	25.15
1.0	1.414213562373095	1.41421356237061	0.7101	6.06×10^{-21}	25.36
3.0	2	1.99999554494570	0.43	2.64×10^{-10}	25.64

5. Results and Discussion

The current results are calculated at $K = m = n = f_w = \delta = 0.5$, $M = \alpha = \lambda = 1$, $Pr = 5$, $\beta = -1$, or otherwise specified in the graph. In Figs. 5–7, the influence of the material parameter (K) is sketched for the horizontal velocity component (f'), transverse velocity (g) and the micro rotational velocity (h) with the increasing value of the similarity variable (η), respectively. When the sheet stretches, prescribed velocities increase with an increase in the concentration of the microparticles in the fluid flow, however, transverse and micro rotational velocities have a reverse impact very close to the stretching sheet. On the other hand, in case of the shrinking sheet, horizontal velocity component and the transverse velocity decrease while the micro rotational velocity increases by increasing the material parameter. Moreover, physical quantities of interest such as local skin frictions, local wall couple stress and heat transfer rate increase in Table 5 and decrease in Table 6 by enhancing the material parameter. Furthermore, Figs. 5–6 are plotted at $\hbar = -0.1$ and in Fig. 7, when sheet stretches, $\hbar = -0.05$ is used and when sheet shrinks $\hbar = -0.015, -0.01, -0.004, -0.002, -0.001$ are set along with the increasing value of the K.

The influence of the buoyancy parameter (λ) is illustrated on the horizontal velocity component in Fig. 8. When either the sheet stretches or shrinks, it shows that an increase in the buoyancy force, alternatively, a decrease in the viscous force yields an increase in the horizontal velocity component. However, as the buoyancy parameter increases, local skin frictions, local wall couple stress and local Nusselt

number increase as shown in Tables 7–8 for stretching and shrinking cases, but local wall couple stress decreases in Table 8. It is to be noted that $\hbar = -0.1$ is used to plot Fig. 8.

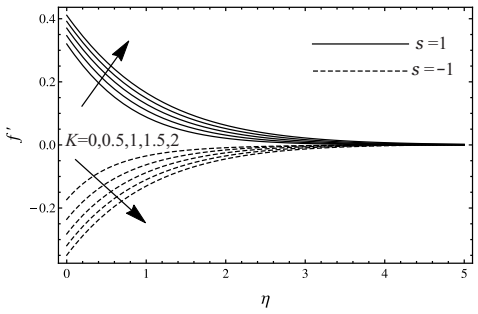

Fig. 5. Impact of K on horizontal velocity component

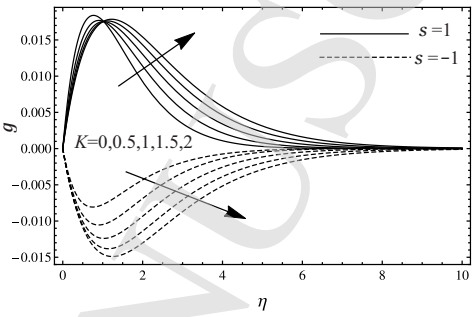

Fig. 6. Impact of K on transverse velocity

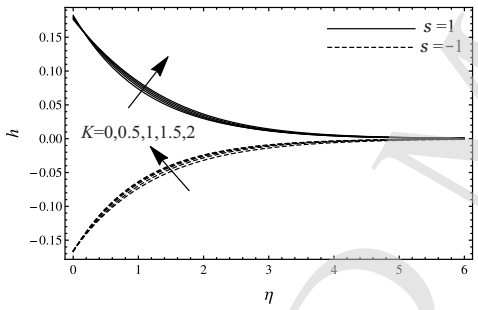

Fig. 7. Impact of K on microrotational velocity

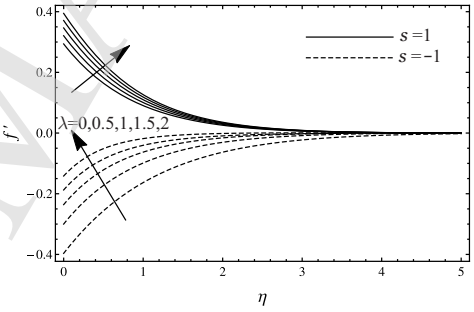

Fig. 8. Impact of λ on horizontal velocity component

Figs. 9–12 display the effect of the transverse magnetic field and the Hall effect parameters on the f' and g at $\hbar = -0.1$. A variation in the magnetic field parameter with the fixed viscosity of the microparticles, i.e., at $K = 0.5$, results in a decrease in the horizontal velocity component and transverse velocity with the stretching sheet and when the sheet shrinks, both prescribed velocities increase. From Figs. 11–12, it is observed that the increasing value of the magnetic field parameter exerts a normal force on the moving microparticles and that force causes to reduce the horizontal velocity component, even with the increasing value of the Hall parameter (as depicted in Fig. 11) and consequently, that normal force reinforces the increasing value of the Hall parameter (in Fig. 12) and thus, it causes an increase in the transverse velocity of the micropolar fluid flow as shown in Fig. 12, in the case of the stretching sheet. It is also noted that at the higher value of the magnetic field ($M = 7$), velocity boundary layer thickness is greater than that of the lower magnetic

field ($M = 1$) in Fig. 12, which supports the assumptions. However, when the sheet shrinks, an increase in the Hall parameter yields a decrease in the horizontal velocity component and transverse velocity. It is worth mentioning that at $M = 0$ in Fig. 10 and at $m = 0$ in Fig. 12 the transverse velocity component is zero for both cases of the sheet which reveals the correctness of our obtained results. Tables 7–8 show that as sheet stretches, increasing value of the transverse magnetic field parameter causes to decrease the local skin friction ($C_{f_x} Re_x^{1/2}$) and heat transfer rate while it increases the local skin friction ($C_{f_z} Re_x^{1/2}$) and local wall couple stress. In addition a reverse trend has been observed in case of the shrinking sheet. Similarly, all physical quantities increase as the Hall parameter increases for $s = 1$ as illustrated in Table 5. Local skin frictions and local Nusselt number decrease and the local wall couple stress increases at $s = -1$ as tabulated in Table 6.

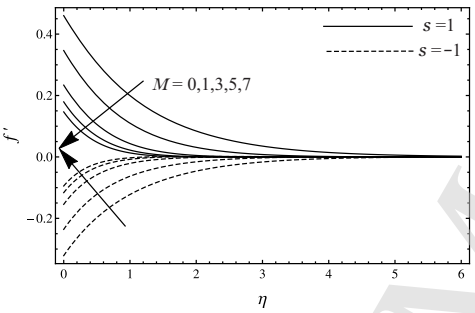

Fig. 9. Impact of M on horizontal velocity component

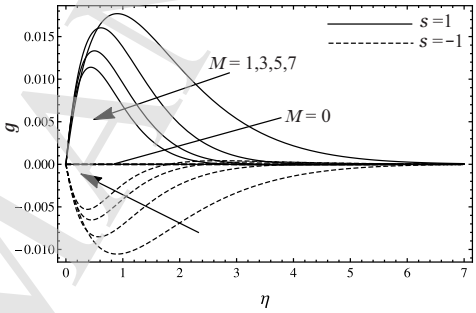

Fig. 10. Impact of M on transverse velocity

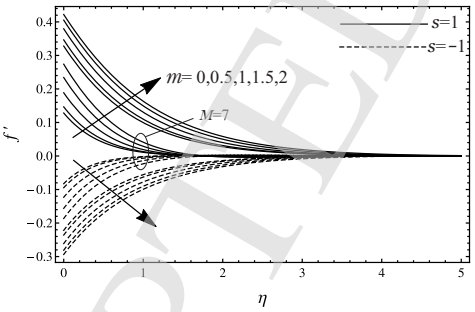

Fig. 11. Impact of m on horizontal velocity component

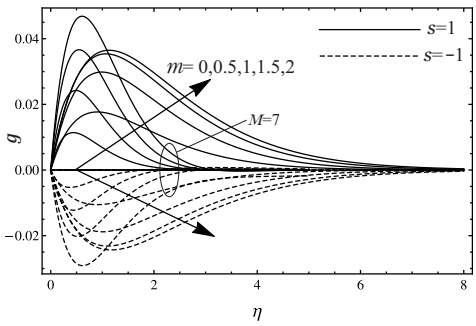

Fig. 12. Impact of m on transverse velocity

Fig. 13 shows the effect of Prandtl number (Pr) on the thermal boundary layer thickness of the micropolar fluid flow. It displays that an increase in the Pr, i.e. an increase in the momentum diffusivity, causes a decrease in the thermal boundary

layer thickness. This results in the reducing temperature of the micropolar fluid flow. This impact is observed at various values of $Pr = 0.1, 0.71, 1, 5, 10, 20, 50, 100, 500$ corresponding to various values of $\hbar = -0.01, -0.01, -0.01, -0.001, -0.001, -0.001, -0.0006, -0.0004, -0.0001$, respectively. However, in Fig. 13 $Pr = 5$ and $\hbar = -0.0001$ are chosen for $s = -1$ (dashed line). It is noted that the local skin friction $(C_{f_x} Re_x^{1/2})$, local wall couple stress and local Nusselt number increase with an increase in the Pr while a decrease is observed in the local skin friction $(C_{f_z} Re_x^{1/2})$ as the sheet stretches in Table 7. Furthermore, when the sheet shrinks (in Table 8), local skin frictions and heat transfer rate increase and local wall couple stress decreases as the Prandtl number increases.

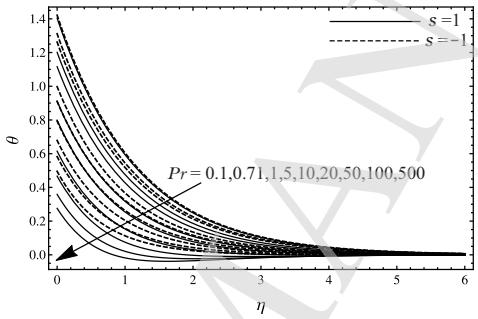

Fig. 13. Impact of Pr on temperature

To investigate the impact of suction $(f_w > 0)$/injection $(f_w < 0)$ parameter, $\hbar = -0.01$ is used in Fig. 14. As predicted, at the constant magnetic field $(M = 1)$, Hall current $(m = 0.5)$ and viscosity of the micro-particles $(K = 0.5)$, the increasing value of the suction parameter causes to reduce the horizontal velocity component while it raises with an increase of the injection parameter with the stretching and shrinking of the sheet as shown in Fig. 14. An increasing value of the suction parameter gives an increase in the local skin friction $(C_{f_x} Re_x^{1/2})$, local wall couple stress and local Nusselt number while it causes a decrease in the local skin friction $(C_{f_z} Re_x^{1/2})$, as the sheet stretches. An opposite trend is noted in the case of an increasing value of the injection parameter in Table 7. However, on the other hand, local skin friction $(C_{f_x} Re_x^{1/2})$ and heat transfer rate increase, and local skin friction $(C_{f_z} Re_x^{1/2})$ and local wall couple stress decrease as the suction parameter increases by shrinking the sheet, and a reverse effect is observed by increasing the injection parameter in Table 8.

Figs. 15–16 depict that the horizontal velocity component decreases with an increase in the first order and the second order slip flow parameters for $s = 1$. This enhancement in the slip flow parameters causes to divert the fluid particles towards the stretching sheet and thus reduces the micropolar fluid flow. Alternatively, when the sheet shrinks, horizontal velocity component increases with an increase of the

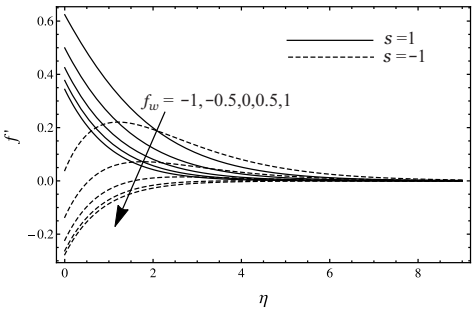

Fig. 14. Impact of f_w on horizontal velocity component

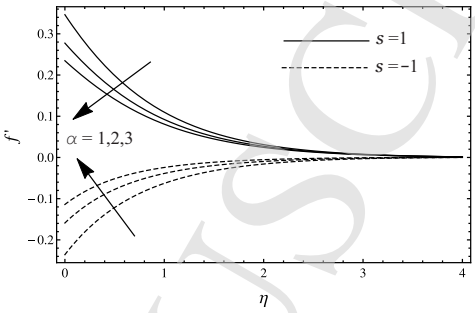

Fig. 15. Impact of α on horizontal velocity component

slip parameters. These results are plotted at $\hbar = -0.1$. From Tables 7–8, it is clear that all of the physical quantities increase when the sheet shrinks and decrease when it stretches.

The influence of the Newtonian heating parameter is sketched in Fig. 17 by fixing $\hbar = -0.1$ except for $\delta = 0.99$ and $\delta = 2$, $\hbar = -0.0048$ and $\hbar = -0.02$ for the stretching sheet and $\hbar = -0.0059$ and $\hbar = -0.005$ for the shrinking sheet, respectively. It displays that a small increment in the Newtonian heating parameter significantly enhances the thermal boundary layer thickness which leads to a raise in the temperature of the micopolar fluid flow. A shrinking sheet produces a higher thermal boundary layer thickness as compared to a stretching sheet as depicted in Fig. 17. On the other hand, when Newtonian heating parameter δ gets a value greater than 1 then the temperature of the micropolar fluid flow decreases which is a significant representation of the initial solution. Moreover, all physical quantities increase with an increase in the Newtonian heating parameter, except the local wall couple stress, which decreases when the sheet shrinks as shown in Tables 7–8.

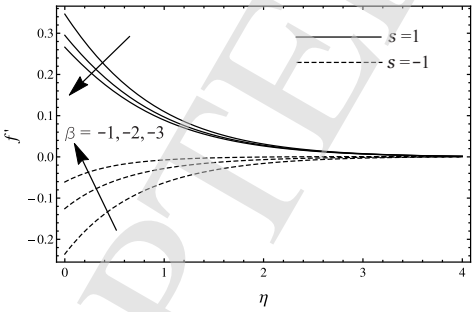

Fig. 16. Impact of β on horizontal velocity component

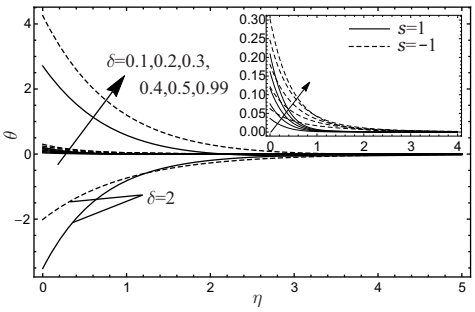

Fig. 17. Impact of δ on temperature

Table 5. Physical quantities for stretching sheet ($s = 1$).

K	M	m	f_w	$C_{f_x}Re_x^{\frac{1}{2}}$	$-\hbar$	$C_{f_z}Re_x^{\frac{1}{2}}$	$-\hbar$	M_xRe_x	$-\hbar$	$Nu_xRe_x^{-\frac{1}{2}}$	$-\hbar$
0.0	1	0.5	0.5	0.369617	0.1	0.0632875	0.1	0.157309	0.1	2.85013	0.1
0.5				0.455632	0.1	0.078183	0.1	0.18582	0.1	2.89193	0.1
1.0				0.540352	0.1	0.0914495	0.1	0.20634	0.1	2.92713	0.1
1.5				0.623147	0.1	0.104336	0.1	0.223985	0.1	2.95723	0.1
2.0				0.703794	0.1	0.117037	0.1	0.239754	0.1	2.98316	0.1
0.5	0			0.446963	0.1	0.000000	0.1	0.179148	0.1	2.09748	0.001
	1			0.442923	0.03	0.078183	0.1	0.18582	0.1	2.09726	0.001
	3			0.433895	0.1	0.103399	0.1	0.186358	0.06	2.09684	0.001
	5			0.405404	0.1	0.105438	0.1	0.189331	0.03	2.09642	0.001
	7			0.380616	0.1	0.108963	0.118	0.190517	0.02	2.09601	0.001
	1	0.0		0.45107	0.1	0.000000	0.1	0.184669	0.1	2.8693	0.1
		0.5		0.455632	0.1	0.078183	0.1	0.18582	0.1	2.89193	0.1
		1.0		0.460024	0.1	0.120246	0.1	0.186447	0.1	2.93337	0.1
		1.5		0.460667	0.1	0.131596	0.1	0.188424	0.03	2.96714	0.1
		2.0		0.465851	0.1	0.169617	0.245	0.195898	0.01	2.99001	0.1
		0.5	1.0	0.426016	0.01	0.0332594	0.01	0.215442	0.01	1.73923	0.005
			0.5	0.423613	0.01	0.0364445	0.01	0.196633	0.01	1.28265	0.005
			0.0	0.417466	0.01	0.0407886	0.01	0.176035	0.01	0.992377	0.005
			-0.5	0.40432	0.01	0.0470598	0.01	0.152113	0.01	0.809874	0.005
			-1.0	0.377978	0.01	0.0565559	0.01	0.121944	0.01	0.695655	0.005

Table 6. Physical quantities for shrinking sheet ($s = -1$).

K	M	m	f_w	$C_{f_x}Re_x^{\frac{1}{2}}$	$-\hbar$	$C_{f_z}Re_x^{\frac{1}{2}}$	$-\hbar$	M_xRe_x	$-\hbar$	$Nu_xRe_x^{-\frac{1}{2}}$	$-\hbar$
0.0	1	0.5	0.5	-0.295306	0.1	-0.029743	0.1	-0.058425	0.1	2.33375	0.1
0.5				-0.396235	0.1	-0.048129	0.1	-0.126233	0.1	2.15285	0.1
1.0				-0.492185	0.1	-0.065651	0.1	-0.154707	0.1	2.00842	0.1
1.5				-0.583877	0.1	-0.082133	0.1	-0.174272	0.1	1.88315	0.1
2.0				-0.671885	0.1	-0.097418	0.1	-0.189906	0.1	1.7715	0.1
0.5	0			-0.400507	0.1	0.000000	0.1	-0.101686	0.1	2.02731	0.001
	1			-0.396235	0.1	-0.048129	0.1	-0.126233	0.1	2.0275	0.001
	3			-0.369586	0.1	-0.059503	0.1	-0.140535	0.1	2.02789	0.001
	5			-0.344537	0.1	-0.071222	0.01	-0.157729	0.03	2.02827	0.001
	7			-0.323887	0.1	-0.107013	0.135	-0.164345	0.02	2.02865	0.001
	1	0.0		-0.391719	0.1	0.000000	0.1	-0.128789	0.1	2.19489	0.1
		0.5		-0.396235	0.1	-0.048129	0.1	-0.126233	0.1	2.15285	0.1
		1.0		-0.401874	0.1	-0.076719	0.1	-0.120608	0.1	2.0675	0.1
		1.5		-0.403932	0.1	-0.086052	0.1	-0.115299	0.1	1.99456	0.1
		2.0		-0.40406	0.1	-0.099660	0.16	-0.111457	0.1	1.94567	0.1
		0.5	1.0	-0.410131	0.01	-0.026517	0.01	-0.205988	0.01	1.44516	0.005
			0.5	-0.416129	0.01	-0.025089	0.01	-0.176774	0.01	1.07763	0.005
			0.0	-0.428294	0.01	-0.021794	0.01	-0.167274	0.001	0.855197	0.005
			-0.5	-0.452639	0.01	-0.01533	0.01	-0.165082	0.01	0.720159	0.005
			-1.0	-0.50051	0.01	-0.003515	0.01	-0.163873	0.008	0.637676	0.005

Table 7. Physical quantities for stretching sheet ($s = 1$).

δ	λ	Pr	α	β	$C_{f_x}Re_x^{\frac{1}{2}}$	$-\hbar$	$C_{f_z}Re_x^{\frac{1}{2}}$	$-\hbar$	M_xRe_x	$-\hbar$	$Nu_xRe_x^{-\frac{1}{2}}$	$-\hbar$
0.1	1	5	1	-1	0.426964	0.1	0.067429	0.1	0.175053	0.1	2.8382	0.1
0.2					0.433355	0.1	0.069948	0.1	0.177378	0.1	2.85109	0.1
0.3					0.440234	0.1	0.072575	0.1	0.17993	0.1	2.86429	0.1
0.4					0.447643	0.1	0.075317	0.1	0.182735	0.1	2.87789	0.1
0.5					0.455632	0.1	0.078183	0.1	0.18582	0.1	2.89193	0.1
0.5	0.0				0.421024	0.1	0.065009	0.1	0.172935	0.1	1.59661	0.01
	0.5				0.438395	0.1	0.071845	0.1	0.179244	0.1	1.62144	0.01
	1.0				0.455632	0.1	0.078183	0.1	0.18582	0.1	1.6466	0.01
	1.5				0.472738	0.1	0.084101	0.1	0.192628	0.1	1.67208	0.01
	2.0				0.489718	0.1	0.089662	0.1	0.199639	0.1	1.69787	0.01
	0.5	0.1			0.41359	0.01	0.040961	0.01	0.190776	0.01	0.85618	0.01
		0.71			0.415514	0.01	0.040201	0.01	0.191875	0.01	0.91627	0.01
		1			0.416342	0.01	0.037906	0.0095	0.19235	0.01	0.94797	0.01
		5			0.416771	0.001	0.036445	0.01	0.206665	0.001	1.04863	0.001
		10			0.416895	0.001	0.034203	0.01	0.206728	0.001	1.12598	0.001
		20			0.417106	0.001	0.031209	0.0095	0.206836	0.001	1.31313	0.001
		50			0.417516	0.001	0.026413	0.008	0.207484	0.0006	1.57138	0.0006
		100			0.420545	0.01	0.017674	0.005	0.207793	0.0004	1.8937	0.0004
		500			0.422557	0.0031	0.011111	0.003	0.208203	0.0001	2.31303	0.0001
		5	1		0.455632	0.1	0.07818	0.1	0.18582	0.1	2.89193	0.1
			2		0.341856	0.1	0.064748	0.1	0.130589	0.1	2.82473	0.1
			3		0.273342	0.1	0.056193	0.1	0.099005	0.1	2.7812	0.1
			1	-1	0.455632	0.1	0.07818	0.1	0.18582	0.1	2.89193	0.1
				-2	0.370753	0.1	0.068315	0.1	0.144306	0.1	2.84114	0.1
				-3	0.323899	0.1	0.062649	0.1	0.122204	0.1	2.81168	0.1

Table 8. Physical quantities for shrinking sheet ($s = -1$).

δ	λ	Pr	α	β	$C_{f_x}Re_x^{\frac{1}{2}}$	$-\hbar$	$C_{f_z}Re_x^{\frac{1}{2}}$	$-\hbar$	M_xRe_x	$-\hbar$	$Nu_xRe_x^{-\frac{1}{2}}$	$-\hbar$
0.1	1	5	1	-1	-0.423303	0.1	-0.093736	0.1	-0.095189	0.1	1.70189	0.1
0.2					-0.419322	0.1	-0.080313	0.1	-0.104879	0.1	1.85421	0.1
0.3					-0.412915	0.1	-0.069102	0.1	-0.112798	0.1	1.95752	0.1
0.4					-0.405152	0.1	-0.058908	0.1	-0.119681	0.1	2.02653	0.1
0.5					-0.396235	0.1	-0.048129	0.1	-0.126233	0.1	2.15285	0.1
0.5	0.0				-0.424374	0.1	-0.109369	0.1	-0.083748	0.1	1.13641	0.01
	0.5				-0.413703	0.1	-0.070571	0.1	-0.111904	0.1	1.15766	0.01
	1.0				-0.396235	0.1	-0.048129	0.1	-0.126233	0.1	1.1797	0.01
	1.5				-0.376079	0.1	-0.032121	0.1	-0.134286	0.1	1.20255	0.01
	2.0				-0.356838	0.1	-0.022960	0.1	-0.138432	0.1	1.22625	0.01
	0.5	0.1			-0.421904	0.01	-0.019258	0.007	-0.182546	0.009	0.85173	0.01
		0.71			-0.421029	0.01	-0.017629	0.006	-0.190363	0.005	0.88123	0.01
		1			-0.420631	0.01	-0.015567	0.005	-0.200056	0.002	0.89616	0.01
		5			-0.416666	0.001	-0.013287	0.004	-0.203986	0.001	1.01375	0.001
		10			-0.416613	0.001	-0.010514	0.003	-0.204383	0.0009	1.04955	0.001
		20			-0.416514	0.001	-0.007356	0.002	-0.204777	0.0008	1.1301	0.001
		50			-0.416265	0.001	-0.003843	0.001	-0.205603	0.0006	1.23687	0.0006
		100			-0.415982	0.001	-0.00349	0.0009	-0.206482	0.0004	1.35825	0.0004
		500			-0.415821	0.001	-0.00314	0.0008	-0.207862	0.0001	1.50909	0.0001
		5	1		-0.396235	0.1	-0.048129	0.1	-0.126233	0.1	2.15285	0.1
			2		-0.292988	0.1	-0.030439	0.1	-0.102509	0.1	2.27437	0.1
			3		-0.232866	0.1	-0.02006	0.1	-0.086858	0.1	2.34015	0.1
			1	-1	-0.396235	0.1	-0.048129	0.1	-0.126233	0.1	2.15285	0.1
				-2	-0.247812	0.1	-0.022584	0.1	-0.090816	0.1	2.32714	0.1
				-3	-0.160294	0.1	-0.00777	0.1	-0.065865	0.1	2.41082	0.1

6. Conclusion

In this investigation, the Hall current effect on the mixed convective magneto-micropolar fluid flow passing over a stretching/shrinking porous sheet has been analysed under the influence of the Newtonian heating. Slip flow condition is also considered in this study. The governing equations of the proposed flow model are transformed and then solved by an approximate analytical technique, named Optimal Homotopy Analysis Method. The proposed model was validated with the similar fluid flow model for the special cases and found to be good in comparison. From the present results, the following conclusion can be made:

- When the sheet stretches with the constant concentration of the micro-elements, increasing value of the magnetic field parameter slows down the horizontal velocity component and the transverse velocity of the micropolar fluid flow, oppositely, an increase in the Hall current parameter not only yields a raise in the horizontal velocity component but also leads to an increase in the transverse velocity. Reverse and similar patterns are observed

for the magnetic field and Hall parameters as in the case of the shrinking sheet, respectively.

- An increasing value of the Newtonian heating parameter increases the fluid temperature and heat transfer rate.
- Furthermore, higher value of the first order or the second order slip flow parameters, horizontal velocity component decreases as the sheet stretches and it increases as the sheet shrinks.
- However, in comparison with the stretching sheet, an increasing magnitude of the Prandtl number rapidly decreases the fluid temperature of the porous sheet. It is noted that it reduces more temperature with heat transfer rate of 93% in contrast to the shrinking sheet.
- The present study can be analysed on the horizontal circular cylinder.

Acknowledgment

The current investigation is funded by Spk:319299-Ver 1, 6353 Curtin University and it does not have any conflict of interest with any researcher.

References

1. A.C. Eringen, *Int. J. Eng. Sci.* **2**, 205 (1964).
2. A.C. Eringen, *J. Math. Mech.* **16**, 1 (1966).
3. A.J. Willson, *Pro. Mathematical Proceedings of the Cambridge Philosophical Society, Great Britain* **67**, 469 (1970).
4. Y. Kazakia and T. Ariman, *Rheol. Acta* **10**, 319 (1971).
5. A.C. Eringen, *J. Math. Anal. Appl.* **38**, 480 (1972).
6. G. Lukaszewicz, *Micropolar Fluids: Theory and Applications* (Springer Science & Business Media, New York, 1999).
7. A.C. Eringen, *Microcontinuum Field Theories: II Fluent Media* (Springer Science & Business Media, New York, 2001).
8. A. A. Bakr and A. J. Chamkha, *Heat Transf Res* **48**, 139 (2017).
9. M. Ashraf and M. M. Ashraf, *Appl. Math. Mech.* **32**, 45 (2011).
10. D. Pal and G. Mandal, *Int. J. Mech. Sci.* **126** 308 (2017).
11. J. Sui, P. Zhao, Z. Cheng, L. Zheng and X. Zhang, *Phys Fluid* **29**, 023105 (2017).
12. A. Mahmood, B. Chen and A. Ghaffari, *J. Magn Magn Mater* **416**, 329 (2016).
13. N.S. Gibanov, M.A. Sheremet and I. Pop, *J. Mol. Liq.* **221**, 518 (2016).
14. M. Muthtamilselvan, K. Periyadurai and D. H. Doh, *Adv. Powder Technol.* **29**, 678 (2018).
15. I. V. Miroshnichenko, M. A. Sheremet, I. Pop and A. Ishak, *Int. J. Mech. Sci.* **128**, 541 (2017).
16. C.L. Chang, *Commun. Nonlinear Sci. Num. Simul.* **13**, 624 (2008).
17. C.L. Chang, *Int. Commun. Heat Mass Transf.* **38**, 429 (2011).
18. Y. Amirat and K. Hamdache, *Nonlinear Anal-Theor.* **102**, 186 (2014).
19. E.M. Abo-Eldahab and M.A. El Aziz, *Inter. Commun. Heat Mass Transf.* **31**, 751 (2004).
20. N. Rani and S.K. Tomar, *Appl. Math. Model.* **34**, 508 (2010).
21. D. Pal, B. Talukdar, I.S. Shivakumara and K. Vajravelu, *Chem. Eng. Commun.* **199**, 943 (2012).

22. X. Yang and L. Wang, *Int. J. Modern Phy. C* **28**, 1750138 (2017).
23. L. Wu, *Appl. Phys. Letter* **93**, 253103 (2008).
24. T. Fang, S. Yao, J. Zhang and A. Aziz, *Commun. Nonlinear Sci. Num. Simul.* **15**, 1831 (2010).
25. M.M. Nandeppanavar, K. Vajravelu, M.S. Abel and M.N. Siddalingappa, *Int. J. Therm. Sci.* **58**, 143 (2012).
26. G. Singh and A.J. Chamkha, *Ain Shams Eng. J.* **4**, 911 (2013).
27. M. Turkyilmazoglu, *Computer Fluid* **71**, 426 (2013).
28. N.C. Rosca and I. Pop, *Eur. J. Mech. B-Fluid* **48**, 115 (2014).
29. R. Sharma, A. Ishak and I. Pop, *J. Aerospace Eng.* **29**, 04016025 (2016).
30. W. Ibrahim, *J. Brazilian Soc. Mech. Sci. Eng.* **39**, 791 (2017).
31. G.W. Sutton and A. Sherman, *Engineering Magnetohydrodynamics* (McGraw-Hill, New York, 1965).
32. J.H. Merkin, *Int. J. Heat Fluid Flow* **15**, 392 (1994).
33. I. Pop and T. Watanabe, *Int. J. Eng. Sci.* **32**, 1903 (1994).
34. W. Hughes, B. John and W. Nicholas, *Schaum's Outline of Fluid Dynamics* (McGraw Hill, 1999).
35. G. Ahmadi, *Int. J. Eng. Sci.* **14**, 639 (1976).
36. M.Kamran, B. Wiwatanapataphee, *Eur. J. Mech. B-Fluid* **71** 138 (2018).
37. S.J. Liao, The proposed homotopy analysis technique for the solution of nonlinear problems, Ph.D. thesis, Shanghai Jiao Tong University, 1992.
38. S.J. Liao, *Beyond Perturbation: Introduction to the Homotopy Analysis Method* (Chapman and Hall: Boca Raton, 2003).
39. S.J. Liao, *Homotopy analysis method in nonlinear differential equations* (Beijing: Higher education press, 2012).